RSC Advances

PAPER

View Article Online
View Journal | View Issue

Cite this: *RSC Adv.*, 2025, **15**, 46402

Temperature-dependent dielectric response and charge transport mechanisms in silicon nanowires for nanoelectronic and sensing applications

W. Gtari,[a] M. Radaoui, *[ab] M. Saadi,[c] N. Nafie,[d] A. Ben Fredj[b] and S. Romdhane[b]

Received 20th August 2025
Accepted 20th November 2025

DOI: 10.1039/d5ra06144j

rsc.li/rsc-advances

Silicon nanowires (SiNWs) have emerged as promising candidates for next-generation nanoelectronic and energy devices due to their tunable physical properties and high surface-to-volume ratio. This work aims to investigate the dielectric response of SiNWs fabricated *via* metal-assisted chemical etching (MACE) of crystalline silicon in $AgNO_3$-based solutions, with particular emphasis on the influence of etching temperature over a fixed etching duration of 20 minutes. Impedance spectroscopy was employed across a broad frequency range (100 Hz–1 MHz) to extract key dielectric and electrical parameters, including complex impedance (Z^*), dielectric loss (ε''), loss tangent ($\tan\delta$), and complex electric modulus (M^*). The impedance behavior was accurately modeled using an equivalent circuit comprising a parallel resistor-CPE network in series with a resistance, revealing interfacial and bulk contributions. AC conductivity followed Jonscher's universal power law, with a temperature-dependent exponent s supporting a thermally activated transport mechanism governed by the non-overlapping small polaron tunneling (NSPT) model. Relaxation peaks in $\tan\delta$ and M'' spectra indicated dipolar polarization and dual relaxation processes, respectively, while low-frequency suppression in M' signified long-range charge mobility. The activation energy extracted from dielectric relaxation aligned closely with that obtained from DC conductivity, affirming the consistency of conduction and relaxation dynamics. These findings contribute to a deeper understanding of charge transport mechanisms in SiNWs and provide valuable insights for optimizing their performance in dielectric and nanoelectronic applications.

1 Introduction

Over the past decade, silicon-based nanomaterials, particularly silicon nanowires (SiNWs)[1–3] and silicon nanoparticles,[4–6] have garnered extensive research attention due to their unique physicochemical properties at the nanoscale. This growing interest is not merely academic; it is driven by the urgent need for scalable, efficient, and miniaturized components for next-generation technologies. Among these, SiNWs have emerged as a particularly promising class of nanostructures owing to their outstanding electronic properties and their tunability through precise control of size, morphology, and doping. As a result, SiNWs hold tremendous potential in advanced nanoelectronics[7,8] and optoelectronic applications.[9] By engineering the growth parameters, the morphology, crystallinity, and doping profiles of SiNWs can be finely tailored to meet the demands of a wide range of functional devices. These include field-effect transistors,[10,11] integrated logic circuits,[12] lithium-ion batteries,[13] photovoltaic devices,[9,14] and systems for photoelectrochemical energy conversion.[15,16] Notably, their nanoscale dimensions, typically in the range of tens to hundreds of nanometers, render SiNWs highly compatible with chemical and biological systems, enabling their integration into life science applications. This includes ultrasensitive molecular detection in biomedical diagnostics,[17,18] as well as real-time bio-interfacing with living cells, tissues, and *in vivo* environments.[19,20] Various fabrication techniques have been developed to synthesize SiNWs, including vapor liquid solid (VLS) growth,[21] electron beam lithography (EBL),[22] focused ion beam (FIB) milling,[23] deep reactive ion etching (DRIE),[24] and metal-assisted chemical etching (MACE).[25] Among these, MACE stands out due to its cost-effectiveness, relative simplicity, and capability to produce vertically aligned, high-aspect-ratio SiNWs with tunable structural parameters.[25] Despite the breadth of research, a detailed understanding of the dielectric and electrical behavior of p-type SiNWs under varying thermal conditions remains insufficiently explored. Temperature-dependent studies of their transport properties are critical to elucidating charge carrier dynamics, trap states, and activation

[a]*Université de Gafsa, Faculté des Sciences de Gafsa, Département de Physique, Campus Sidi Ahmed Zarouk, Gafsa, 2112, Tunisia*

[b]*Laboratoire Matériaux Avancés et Phénomènes Quantiques, Faculté des Sciences de Tunis, Université de Tunis El Manar, 2092 Campus Universitaire, Tunis, Tunisia. E-mail: raddaouimoufid@gmail.com*

[c]*Université de Tunis El Manar, LMOP (LR99ES17), Tunis, 2092, Tunisia*

[d]*Laboratoire de Photovoltaïque, Centre de Recherches et des Technologies de l'Energie, BP 95 Hammam-Lif 2050, Tunisia*

mechanisms, which are key to optimizing their performance in practical electronic and sensor applications.[9,21] The present study aims to address this gap by systematically investigating the temperature-dependent dielectric properties of SiNWs fabricated by metal-assisted chemical etching (MACE), with a fixed etching duration of 20 minutes. Specifically, it seeks to extract and interpret frequency- and temperature-dependent electrical parameters, such as complex impedance (Z), dielectric loss (ε''), loss tangent ($\tan\delta$), and complex electric modulus (M^*), in order to gain insight into the conduction mechanisms and relaxation dynamics occurring within these nanostructures. Although SiNWs synthesized by MACE have been previously reported in the literature, including studies focusing on their electrical and optical properties nearly a decade ago, renewed investigation is warranted for several reasons. First, advances in nanofabrication and characterization techniques enable more refined and accurate analysis of nanoscale dielectric behavior. Second, the specific influence of thermal treatment during etching on the dielectric relaxation processes and AC conductivity has not been fully characterized. Third, a systematic impedance spectroscopy-based approach spanning a wide frequency range provides a comprehensive framework to unravel polaronic transport mechanisms and relaxation phenomena that were either overlooked or insufficiently resolved in earlier studies. Accordingly, this work not only revisits a previously explored material system but builds upon it with a distinct focus and methodological rigor aimed at generating new, practically relevant insights. Recent studies on the dielectric and impedance behavior of SiNWs have mainly concentrated on room-temperature or single-frequency analyses, with limited attention to temperature-dependent relaxation dynamics or multi-model interpretation.[26,27] In contrast, the present work provides a comprehensive investigation of p-type SiNWs synthesized by the metal-assisted chemical etching (MACE) technique, combining variable-temperature broadband impedance spectroscopy with multi-scale relaxation analysis and cross-model validation. This integrated approach allows a deeper understanding of thermally activated charge transport and dielectric relaxation processes, thereby highlighting the originality and broader significance of the present study. The results are expected to inform future device optimization strategies and guide the integration of SiNWs into temperature-sensitive nanoelectronic and sensing platforms.

2 Experiment

The synthesis of silicon nanowires (SiNWs) in this work was carried out using the metal-assisted chemical etching (MACE) method, following a previously established protocol.[25] The current study builds upon this method with a new focus on the influence of etching temperature on the dielectric properties of the resulting SiNWs. While, the core etching chemistry and substrate specifications were adapted from earlier work, key innovations in this study include the systematic variation of thermal conditions during etching, followed by detailed impedance spectroscopy-based dielectric analysis, which were not addressed in the prior report. The substrates consisted of boron-doped, p-type (100)-oriented monocrystalline silicon wafers, 500 μm thick, with a resistivity of 0.5–3.0 Ω cm. Prior to etching, wafers underwent a rigorous cleaning process: immersion in boiling acetone for 10 minutes, ethanol rinse for 5 minutes, and three successive rinses in deionized water. Native oxide was removed by dipping in 5% HF solution for 1 minute. The cleaned wafers were then immersed in an etching solution containing 10 ml of 23.20 M aqueous HF, 10 ml of 0.02 M $AgNO_3$, and 1 ml of 10.00 M H_2O_2. The etching was conducted for a fixed duration of 20 minutes, while the temperature was systematically varied (as discussed in Section 3). Following etching, the substrates were treated with 44% HNO_3 to remove residual silver dendrites and rinsed with deionized water. The resulting vertically aligned SiNWs were structurally similar to those previously reported.[25] In fact, the SEM image presented in Fig. 2 corresponds to a micrograph acquired during the earlier study,[25] and is reused for representational consistency, as the morphology of the SiNWs remained comparable under the base etching conditions. After the fabrication of silicon nanowires (SiNWs), silver (Ag) layers approximately 2 μm thick were deposited on both the front and back surfaces of the SiNWs/Si substrate using the screen-printing (serigraphic) technique. In this process, a commercial Ag paste was uniformly applied through a stainless-steel mesh using a squeegee. The printed samples were then subjected to a thermal treatment at 550 °C for 10 minutes in an infrared furnace to remove the organic binders and to promote the diffusion and sintering of Ag particles, leading to a continuous conductive film. This procedure resulted in the formation of a Ag/Si/SiNWs/Ag layered structure with good electrical contact between the Ag electrodes and the silicon substrate. The final device configuration, Ag/Si/SiNWs/Ag, is schematically shown in Fig. 1. These devices were used for temperature-dependent dielectric and electrical measurements, as detailed in Section 3.

The sample morphology was analyzed using a scanning electron microscope (SEM) in order to study the structural quality of the SiNWs. The average diameter of the SiNWs (~100 nm) was estimated from high-magnification top-view SEM images by measuring the lateral widths of several nanowire tips. The extended error of this measurement is estimated to 2%.[25]

Dielectric properties were measured with a Solartron 1260A Impedance Analyzer coupled with 1296A Dielectric Interface in the 100–10^6 Hz frequency range. Measurements were performed over a wide temperature range, from room temperature up to 325 °C in 50 °C increments, using a Linkam hot-stage during the impedance and dielectric experiments.

3 Results and discussions

3.1 Impedance spectroscopy analysis

Fig. 2(a) shows the Nyquist plot for Ag/Si/SiNWs/Ag sample obtained by plotting the imaginary part of the complex impedance *versus* the real part measured at different temperature. The generated plots exhibit semi-circular shapes that are slightly depressed towards the Z' axis. As the temperature increases, the size of these semi-circles decreases, indicating the semiconductor characteristics of the material.[28] Fig. 2(b)

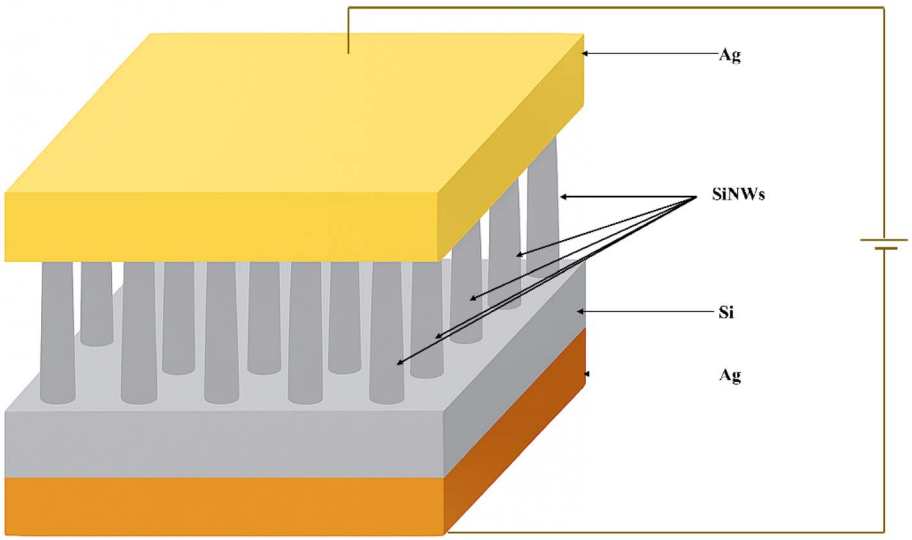

Fig. 1 Schematic representation of Ag/Si/SiNWs/Ag structure.

shows the variation of real part of the impedance (Z') with frequency at different temperatures. We note that the value of Z' decreases with rise of both frequency and temperature which suggests an increase in the ac conductivity. The Z' *versus* frequency plot illustrates an upward dip in the Z' values before reaching a merging point at high frequencies. This behavior is likely attributed to the hopping of charge carriers and the subsequent release of space charge polarization. These processes contribute to reducing the barrier within the material.[29] In Fig. 2(c), it is observed that the maximum Imaginary impedance spectra Z'' shifts to high frequency, with increase in temperature, in which the resistance of the sample decreases, hence the electrical conductivity increases.[30] Such behavior indicates the presence of electronic relaxation in the system.

To effectively study the impedance spectrum, it's beneficial to have an equivalent circuit model that accurately reflects the electrical characteristics of the different regions. As a result, a parallel RC element (consisting of a bulk resistance (R_b) and a parallel capacitor) is employed to represent each semicircle. The presence of a semicircle depression on the graph suggests that the capacitor can be replaced with a constant phase element (CPE), which has an impedance represented by: $Z_{CPE} = \frac{1}{A_0(j\omega)^n}$,[31,32] where j is the imaginary unit ($j^2 = -1$) and ω is the angular frequency ($\omega = 2\pi f$, f is the frequency), A_0 is an independent frequency constant in F.cm^2 s^{n-1},[33] and n ($0 < n < 1$) is a dimensionless parameter that reflects the tendency toward a perfect semi-circle. To ensure the validity of this model, alternative configurations, including the double parallel (R-CPE) and transmission line models, were tested for comparison. However, these models did not significantly improve the fitting accuracy, as the coefficient of determination (R^2) remained consistently high (≈ 0.999) and the residuals showed no systematic deviation. Consequently, the simplified R_S + (R-CPE) circuit was retained, as it provides the most physically meaningful and statistically reliable representation of the electrode-interface-bulk system under study.

The circuit's total impedance is expressed as follows:

$$Z^* = Z' + jZ'' = \left(\frac{1}{R_b} + \frac{1}{Z^*_{CPE}}\right)^{-1} \quad (1)$$

$$Z' = \frac{R_b \times \left(1 + R_b A_0 \omega^n \times \cos\left(\frac{n\pi}{2}\right)\right)}{1 + 2R_b A_0 \omega^n \times \cos\left(\frac{n\pi}{2}\right) + (R_b A_0 \omega^n)^2} \quad (2)$$

$$Z'' = \frac{{R_b}^2 A_0 \omega^n \times \sin\left(\frac{n\pi}{2}\right)}{1 + 2R_b A_0 \omega^n \times \cos\left(\frac{n\pi}{2}\right) + (R_b A_0 \omega^n)^2} \quad (3)$$

where R_b is the bulk resistance.

A theoretical curve fitting and experimental data are measured. A good agreement between the experimental and theoretical curves was attained.

The extract parameters for the circuit elements are collected in Table.

From Table 1, as the temperature increases, the resistance of the sample decreases, resulting in an increase in electrical conductivity. In fact, the increase in temperature causes an increase in thermal energy, which increases the motion of the atoms or particles in the material. This increased motion can lead to a greater number of collisions between the electrons and the lattice ions in the material, which can cause a decrease in the resistance of the material.[34] Furthermore, an increase in temperature can also increase the number of free electrons available for conduction, which can also contribute to a decrease in resistance and an increase in electrical conductivity.[35] The values of n increase with temperature and vary in the range 0.684–0.71, confirming that all the interactions between localized sites are weak.[36] This increase may be due to changes in the electrical properties of the materials involved. As

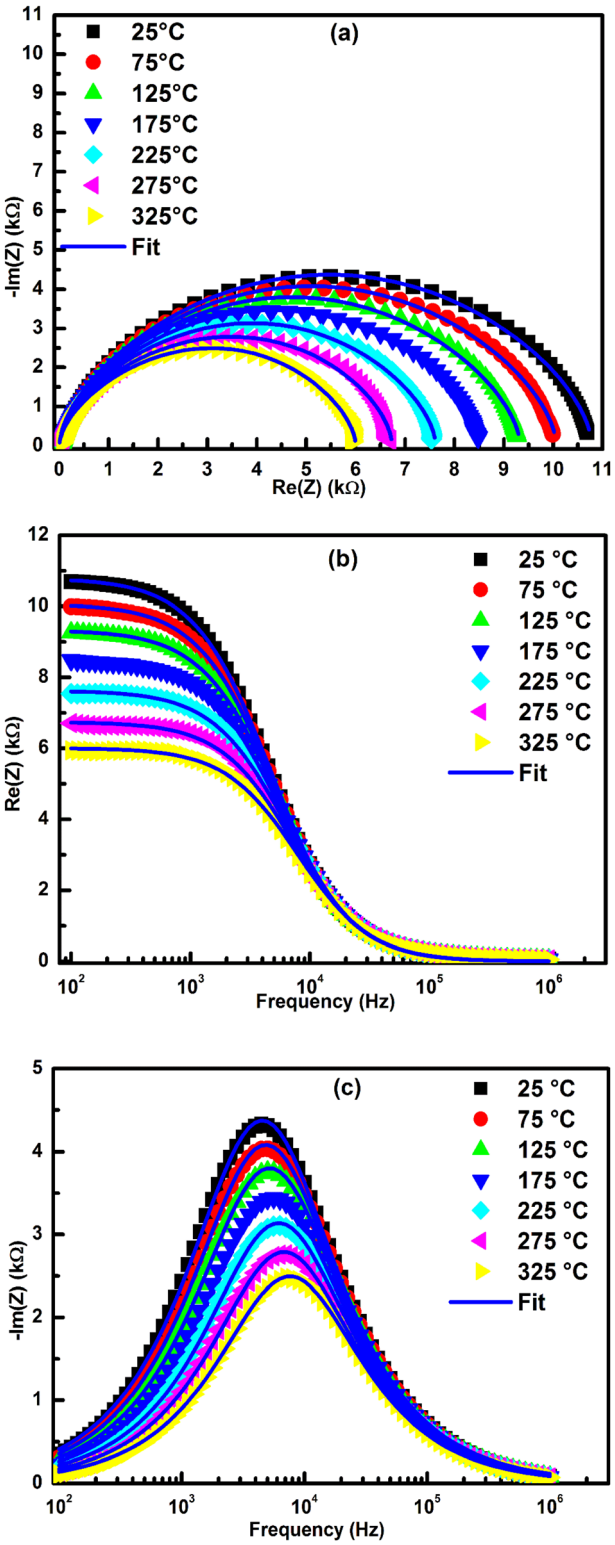

Fig. 2 (a) Nyquist plots (−ImZ *vs.* ReZ), (b) variation of real (Z) and (c) Im (Z) as a function of frequency at different temperatures. Solid lines represent the fit to experimental data using eqn (1) (R-squared∼ 0.999).

the temperature increases, the concentration of free carriers (electrons and holes) in the material also increases, leading to an increase in electrical conductivity.[37] In addition, the surface roughness and interfacial effects at the silicon/silicon nanowires junction may also contribute to the non-ideal behavior of the CPE.[38] These effects become more pronounced at higher temperatures, leading to an increase in the value of n.[39]

Table 1 The best fitting values of equivalent circuit elements at different temperatures

Temperatures (°C)	R_b (kΩ)	A_0 (10^{-11} F cm^2 s^{n-1})	n
25	10.8 ± 0.2	7.15 ± 0.05	0.684 ± 0.002
75	10.1 ± 0.2	6.82 ± 0.05	0.686 ± 0.002
125	9.3 ± 0.2	6.41 ± 0.04	0.688 ± 0.002
175	8.5 ± 0.2	5.87 ± 0.04	0.690 ± 0.002
225	7.6 ± 0.2	4.45 ± 0.03	0.700 ± 0.002
375	6.0 ± 0.1	3.29 ± 0.02	0.710 ± 0.001
325	6.7 ± 0.1	3.31 ± 0.02	0.710 ± 0.001

3.2 Electrical conductivity analysis

The frequency dependence of AC conductivity at various temperatures for the sample is shown in Fig. 3. The conductivity has dispersion at all frequencies. According to this figure, the conductivity spectra can be categorically divided into two regions. Almost constant conductivity values were observed at low-frequency region extending up to a frequency, known as the hopping frequency f_{Hop}. Since the conductivity in this range is virtually constant, although the frequency varies, it is often noted σ_{dc}as "direct current" conductivity. According to Fig. 3, σ_{dc} grows with temperature rise which indicates that the conduction process is thermally activated, and the prepared material exhibits semiconductor behavior over the entire temperature range. Above f_{Hop}, the conductivity increases exponentially with frequency. This promotes the conduction process in the sample due to the increase of electrons hopping. The conductivity at frequencies higher than f_{Hop} corresponds to the conductivity in alternating current (σ_{ac}). The phenomenon of the conductivity dispersion is generally analyzed using Jonscher's law:[40]

$$\sigma(\omega) = \sigma_{dc} + A\omega^s \quad (4)$$

where $\sigma_{dc}$is the frequency-independent conductivity, ω is the angular frequency of the applied AC field in the frequency sensitive region, A is a constant which determines the polarizability strength and s is the less critical exponent characterizing hopping conduction constants. The power law has been applied to many materials.[41,42] The above-mentioned equation has been used to fit the conductivity data. In the fitting procedure, A and s values have been varied simultaneously to get the best fits.

The $s(T)$ values plotted in Fig. 3(b) are all higher than unity. Based on the information presented in this figure, it can be inferred that the electrons hopping involves translational movement between neighboring sites. Similar findings have been reported in other studies.[43,44] In addition, an increasing tendency in s values was observed with temperature rise. This is a criterion for a typical thermally activated conduction process. This indicates also that the "non-overlapping small polaron

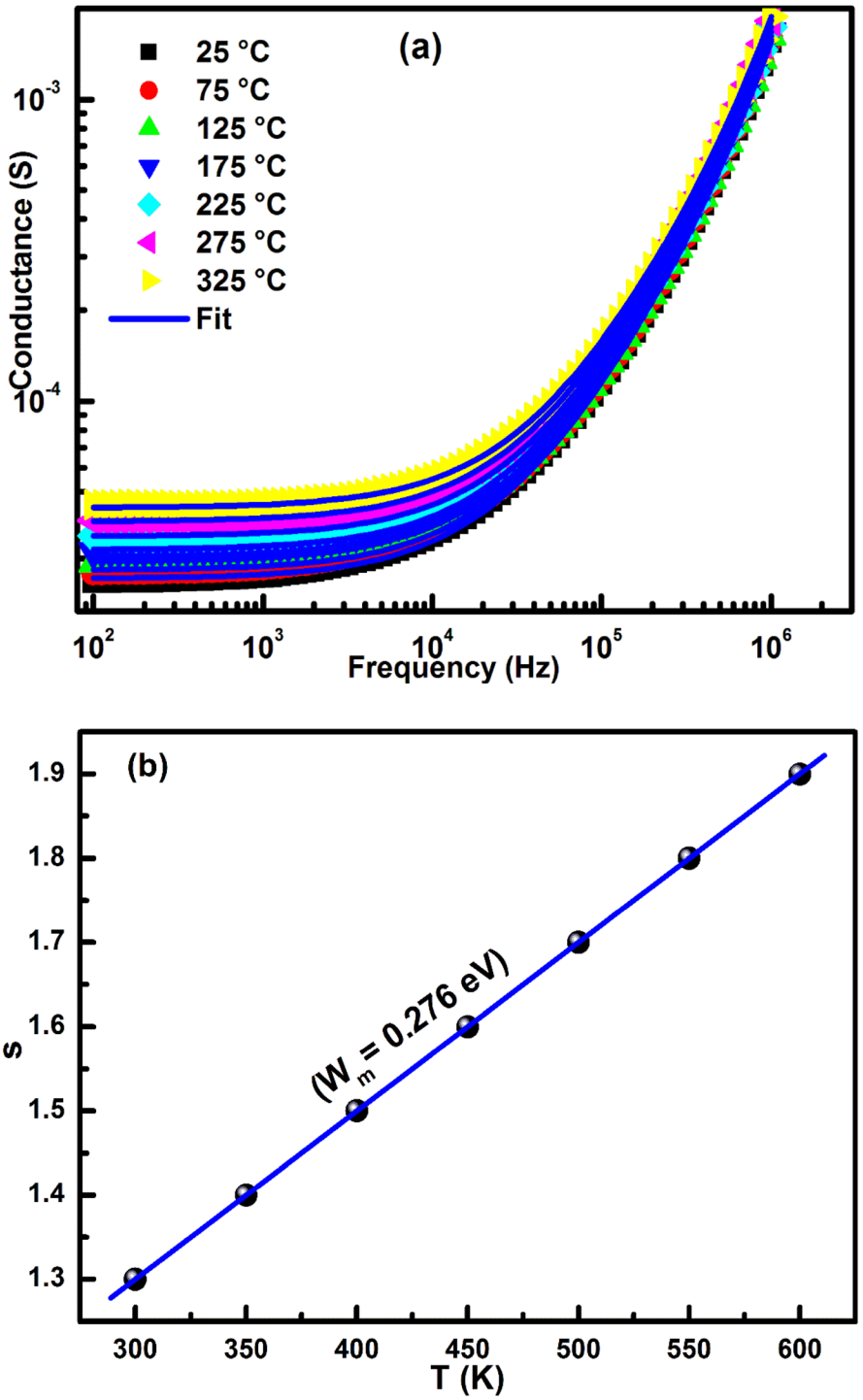

Fig. 3 (a) Variation of the conductivity with angular frequency of the device at different temperatures. Solid lines represent the fits by using eqn (4). (b) Variation of s exponent *vs.* temperature (R-squared~ 0.999).

tunnelling" (NSPT model)[45] is valid in the case of Ag/Si/SiNWs/Ag sample. According to this model, the s exponent can be formulated in eqn (5) as:[45]

$$s = 1 + \frac{4k_B T}{W_m} \quad (5)$$

where k_B is the Boltzmann constant, T is the temperature, and W_m represents the polaron binding energy (*i.e.* the binding energy of the carrier in its localized site). The obtained W_m value is around 0.276 eV.

3.3. Dielectric properties

3.3.1. Permittivity and loss studies. The complex dielectric constant, also known as the complex permittivity or complex relative dielectric constant, is a measure of the ability of

a material to store and dissipate electrical energy as a function of frequency. It is a complex quantity that consists of two components: a real part (ε') and an imaginary part (ε''). The following complex dielectric constant can be used to illustrate the dielectric response of any material:

$$\varepsilon(\omega) = \varepsilon'(\omega) + j\varepsilon''(\omega) \quad (6)$$

Eqn (7) expresses the imaginary part of the dielectric constant:

$$\varepsilon''(\omega) = \frac{Z'}{\omega C_0\left(Z'^2 + Z''^2\right)} \quad (7)$$

where $C_0 = \frac{\varepsilon_0 S}{d}$ ($C_0$is the free space capacitance, $\varepsilon_0$is the permittivity of free space, S refers to the area of the electrode and d is the active layer thickness).

Fig. 4 depicts the frequency dependence of the dielectric loss (ε'') of the device at different temperatures.

Using the Drude model, the dielectric function ε can be calculated as a function of the density of free carriers N:[46]

$$\varepsilon(\omega) = \varepsilon_\infty - \frac{{\omega_p}^2}{\omega(\omega + i\Gamma)} \quad (8)$$

where $\varepsilon_\infty = 11.7$ for silicon, $\omega_p(N)$ is the plasma frequency and a function of the carrier concentration N, and Γ is the damping rate.

There are two regions in the graphical plot of the imaginary part (ε'') of the complex dielectric permittivity *vs.* frequency (f). At the frequency of less than 10^4 Hz, ε'' decreases as f increases for all temperatures. This can be attributable to the deformation and relaxation polarization contributions.[47] Afterwards, for the frequencies greater than 10^4 Hz, as the frequency is increased, the value of ε'' becomes quasi-constant. The significant decrease in ε'' has sparked a lot of interest in this material's possible uses in electrical energy storage. The dielectric loss rises sharply at low frequency when the temperature rises indicating that electrode polarization and space charge effects have occurred confirming non-Debye dependence. Moreover, at low frequencies, the dielectric loss in silicon nanowires can be dominated by the motion of charges and defects at the interfaces between the nanowire and surrounding material. As the temperature of the system rises, the mobility of these charges and defects can increase, leading to an increase in dielectric loss at low frequencies.[48] Extensive research was conducted on the significant reduction in ε'', with the aim of exploring the potential use of these dielectric materials for electrical energy storage.[49,50]

The dielectric loss tangent is a measure of the energy lost as heat when an electric field is applied to a dielectric material. It is defined as the ratio of the imaginary part of the dielectric constant (which represents the energy lost as heat) to the real part of the dielectric constant (which represents the energy stored in the electric field). Mathematically, it is expressed as:

$$\tan(\delta) = \frac{\varepsilon''}{\varepsilon'} \quad (9)$$

where tan δ is the dielectric loss tangent, ε'' is the imaginary part of the dielectric constant, and ε' is the real part of the dielectric constant.

Fig. 5 illustrates the variation in the loss tangent with frequency at different temperatures for Ag/Si/SiNWs/Ag structure.

This figure indicates that tan(δ) increases around 10^5 Hz and then decreases for all temperatures. The peaks observed around up to 10^5 Hz at 25 °C, thus move from 25 °C to 325 °C by step of 4×10^2 Hz for each temperature, which related to the behavior of dipolar polarization.[51] The time taken for the dipoles to come back to its original random orientation is called "the relaxation time τ_{rel}". τ_{rel} is determined from the frequency maximum, f_{max} of tan(δ)peak by the Arrhenius relation:[52]

$$\tau_{rel} = \frac{1}{2\pi f_{max}} \quad (10)$$

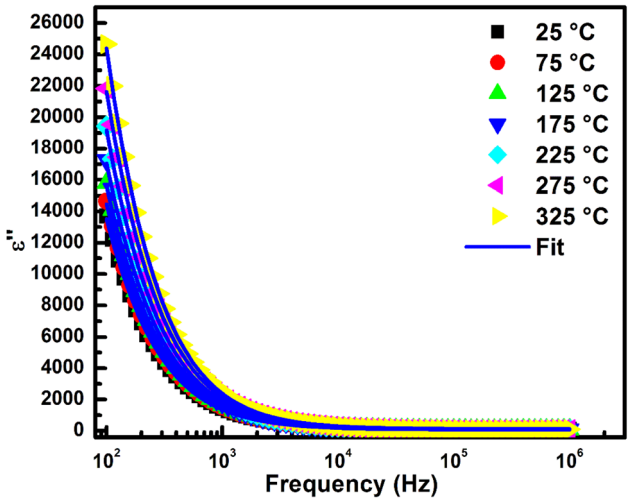

Fig. 4 Dependence of the dielectric loss (ε'') on frequency of the device at different temperatures. Solid lines represent the fits by using eqn (8) (R-squared~ 0.999).

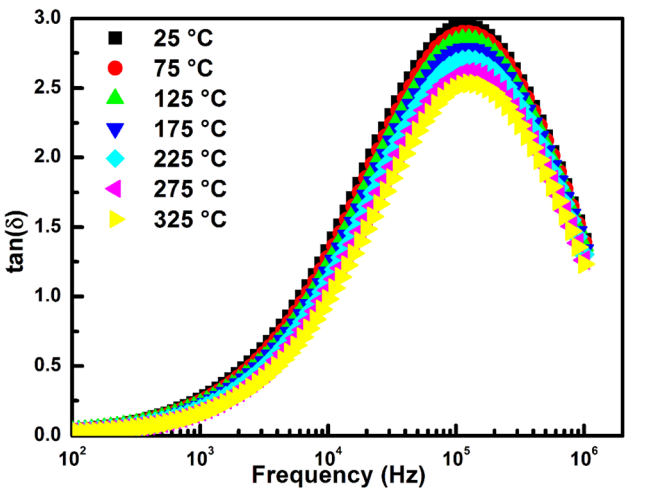

Fig. 5 Dielectric loss tangent,tan(δ), as a function of angular frequency of the device at different temperatures.

It is found that τ_{rel} decreases slightly from 25 °C to 325 °C, this observation pointed out that for the high temperatures took less relaxation time for dipole orientation. Moreover, the reason behind this behavior could be attributed to the increased mobility of charge carriers at higher temperatures. As the temperature rises, the thermal energy increases, which promotes the movement of charges, leading to a decrease in the relaxation time. This result confirms our previous findings.

3.3.2. The electrical modulus formalism. Electrical modulus analysis is a method that is employed to study the electrical characteristics of materials and devices, primarily in the frequency domain. It comprises assessing the material's complex dielectric constant at different frequencies, which can reveal details about its atomic and molecular structure and electronic properties. By analyzing the electrical modulus one can extract valuable insights into the relaxation processes occurring in the material. In-depth analysis of the complex electrical modulus (M^*) formalism offers distinct advantages over traditional permittivity (ε) and conductivity (σ) representations, particularly in systems like SiNWs where interfacial polarization, electrode effects, or significant dc conductivity may mask intrinsic bulk properties. While, ε tends to exaggerate the effects of high capacitance regions such as space charge at interfaces or electrode polarization. M^* suppresses these contributions by inversely weighting the dielectric response, thus enhancing the visibility of bulk relaxation processes. Furthermore, conductivity spectra often show a superimposed dc plateau and ac dispersion, which can obscure subtle relaxation dynamics, especially at low frequencies. In contrast, the M^* formalism shifts the relaxation features to higher frequencies, allowing for a clearer separation between localized hopping, bulk charge transport, and long-range ionic motion. This makes the electrical modulus particularly valuable for identifying relaxation times, probing the spatial distribution of mobile carriers, and detecting thermally activated processes within the nanostructured SiNW matrix. Consequently, M^* analysis provides a more reliable window into the true dielectric relaxation behavior of the material, complementing and enhancing the insights gained from ε and σ spectra.

The electric modulus M^* is expressed as follows:

$$M^* = \frac{1}{\varepsilon^*} = M' + jM'' \tag{11}$$

The real M' and imaginary M'' parts of M^* have been calculated using the following relations:

$$M' = \frac{\varepsilon'}{\varepsilon'^2 + \varepsilon^2}; M'' = \frac{\varepsilon''}{\varepsilon'^2 + \varepsilon''^2} \tag{12}$$

The frequency dependence of M' at various temperatures is shown in Fig. 6(a). At low frequencies, M' value is near zero, which justify the absence of electrode polarization effect.[53] After 1 kHz, it increases with increasing frequency to reach a maximum value around the frequency of 10^6 Hz due to relaxation process.[54] Additionally, an observation was made that the dispersive region of M' shifts towards a frequency of approximately 10^6 Hz as the temperature increases. This observation is consistent with the dielectric response and provides further confirmation of the non-Debye behavior.

Fig. 6(b) shows the imaginary part of modulus (M'') as a function of frequency. This plot provides insight into the bulk

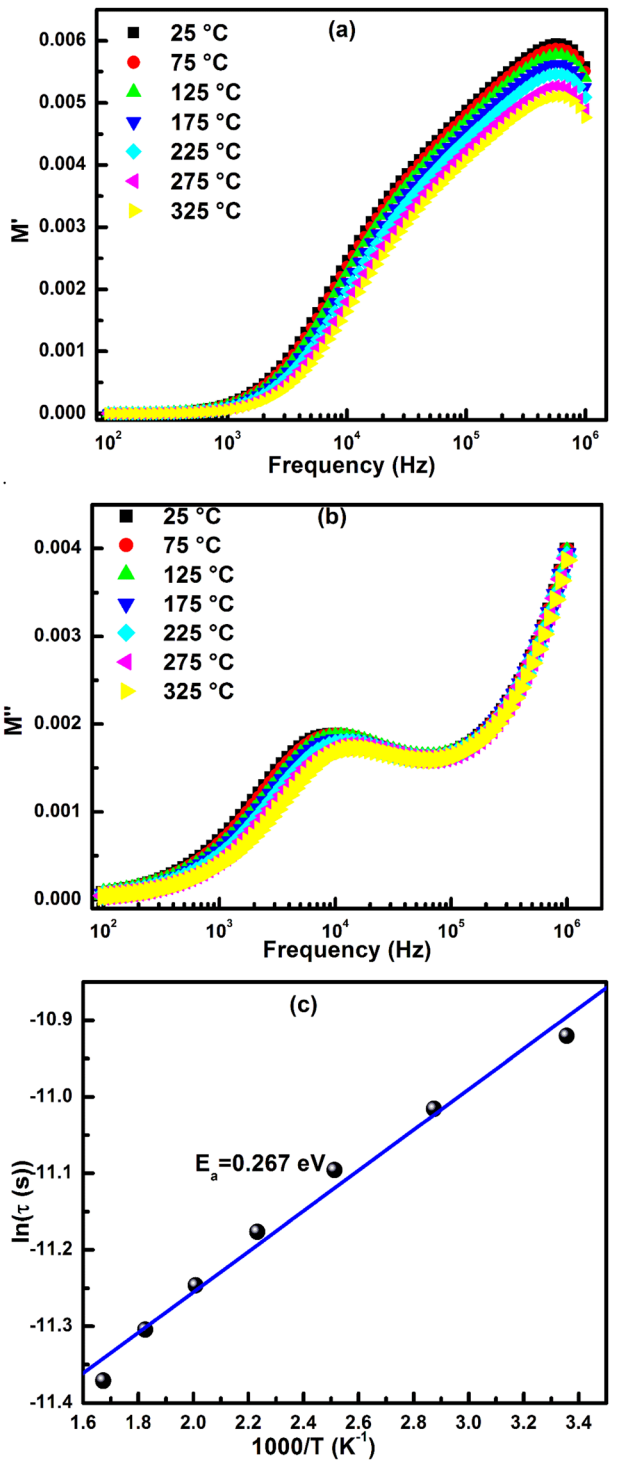

Fig. 6 (a). Frequency dependent plot for real part of modulus (M'), (b) imaginary part of modulus (M'') at various temperatures and (c) variation of relaxation ln(τ) with 1000/T and solid line represents the fitted Arrhenius relation (R-squared~0.992).

properties of materials and indicates a suppression of electrode and interfacial polarization effects due to higher capacitance values.[55] The presence of multiple peaks in the plot indicates dual relaxation phenomena.[56] However, it should be noted that the peak at higher frequency is not fully resolved due to frequency limitations of the system. As the temperature increases, there is a shift in the peak towards higher frequency, which suggests the existence of thermally activated relaxation processes. The frequency region below the relaxation peak indicates the hopping of charge carriers occurring over long distances, while the frequency region above the peak indicates short-range order and the localization of charge carriers within a potential well, where they are free to move inside the well.[57]

As the temperature increases, the peaks in the frequency-dependent data are observed to shift towards higher frequencies. This phenomenon is indicative of thermally activated relaxation processes, which is in agreement with the impedance results. Additionally, the presence of multiple peaks in the data suggests that the sample exhibits non-Debye type relaxation, as reported in previous studies.[58] From these peaks, we extract the relaxation frequency f_{max}, which corresponds to M''_{max} defined condition $\omega_c\tau = 1$ where relaxation time $\tau = \frac{1}{2\pi f_{max}}$. Fig. 6(c) shows the variation of relaxation time *versus* $1000/T$ for the elaborated structure, which follows the relation:[59]

$$\tau = \tau_0 \exp\left(\frac{E_a}{kT}\right) \quad (13)$$

where τ_0 is the pre-exponential factor and E_a is the activation energy for the conductivity relaxation. The activation energy (E_a) calculated from the slope of the line shown in Fig. 6(c) using eqn (13) is found to be approximately 0.267 eV. The similarity between E_a and the activation energy for dc conductivity suggests that the same energy barrier must be overcome by ions during both conduction and relaxation processes. This similarity in activation energies implies that the charge carriers involved in conduction and relaxation are experiencing similar energy landscapes, which could be due to similar microscopic mechanisms underlying these processes.[60] The similarity in activation energies indicates that these localized states or defects are isotropically distributed within the material, meaning that charge carriers can hop through them with equal probability in all directions.

The complex modulus plot (M' *vs.* M'') at different temperatures is shown in Fig. 7. The M' *vs.* M'' plot is often considered more useful than the Z' *vs.* Z'' plot for analyzing specific types of materials and devices. This is because the M' *vs.* M'' plot provides information about the real and imaginary components of the complex modulus, while the Z' *vs.* Z'' plot only provides information about the magnitude and phase of impedance. The M' *vs.* M'' plot is particularly helpful in providing detailed insights into the relaxation processes occurring in a material, which are related to the movement of charges or dipoles in response to an applied electric field. Another benefit of the M' *vs.* M'' plot is its ability to detect subtle changes in the material's behavior across different frequencies, even when the impedance magnitude and phase do not vary significantly. On the other hand, the Z' *vs.* Z'' plot may not always be able to resolve small changes in impedance magnitude and phase. The M' *vs.* M'' plot shows the existence of two successive semi-circular peaks. The first semicircle is attributed to interfacial properties and the second one is associated to the bulk properties. This indicates the existence of two relaxation processes with two relaxation times (τ) for each relaxation.[61]

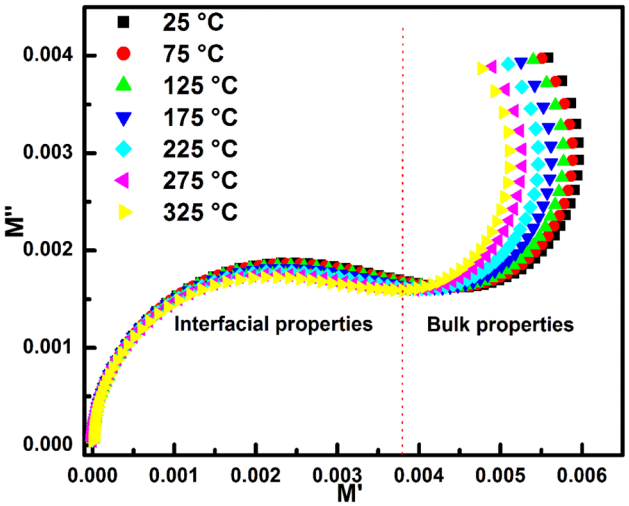

Fig. 7 Variation of M' *vs.* M'' curves at different temperatures for the Ag/Si/SiNWs/Ag structure.

4. Conclusion

In summary, Static, dynamic, and dielectric studies have been investigated in depth on Ag/Si/SiNWs/Ag device. The complex impedance dependence of temperatures is discussed and is modeled in the frequency range of 100 Hz–1 MHz by a constant phase element CPE. AC conductivity plots were analyzed by using Jonscher power law and its dependence of conduction mechanism can be inspired from small polaron model. The values of the dielectric loss (ε''), dielectric loss tangent ($\tan(\delta)$), the real (M'), and the imaginary (M'') parts of the electrical Modulus (M^*) of the device have been determined in the same frequency range used in complex impedance and at different temperature. A decrease of the ε'' with increasing frequency and at different temperatures is observed. At low frequencies, M' and M'' values are near zero, which justify the absence of electrode polarization effect.

The presence of multiple peaks in the M'' *vs.* frequency plots indicates dual relaxation phenomena and exhibits non-Debye type relaxation. We found a similarity between the activation energy determined from the M'' *vs.* frequency plots and the other one for dc conductivity suggests that the same energy barrier must be overcome by ions during both conduction and relaxation processes.

Conflicts of interest

There are no conflicts to declare.

Data availability

All data supporting the findings of this study are available from the corresponding author upon reasonable request.

References

1 B. Chouaibi, M. Radaoui, N. Nafie, A. Ben Fredj, S. Romdhane and H. Bouchriha, Study of magnetoconductance effect in silicon nanowires formed by chemical etching in HF/AgNO3 solution: Effect of etching time, *J. Cryst. Growth*, 2017, **463**, 54–58.

2 B. Chouaibi, M. Radaoui, N. Nafie, A. Ben Fredj, S. Romdhane, M. Bouaïcha and H. Bouchriha, Effect of porosity on the enhancement of relative magnetoconductance in porous Si nanostructures: a comparative study with Si nanowires, *Appl. Phys. A*, 2017, **123**, 489.

3 B. Ben Abdelaziz, M. Radaoui, A. Ben Fredj, S. Romdhane, C. Ben Alaya, M. Bouaïcha and H. Bouchriha, Effect of Etching Time to Tune Magnetoresistance Between Positive and Negative Values in p-Type Silicon Nanowires, *J. Electron. Mater.*, 2019, **48**, 7813–7818.

4 B. Chouaibi, M. Radaoui, A. Benfredj, S. Romdhane, M. Bouaïcha and H. Bouchriha, Porosity dependence of positive magnetoconductance in n-type porous silicon, *Phys. Status Solidi C*, 2012, **9**, 1896–1899.

5 M. Radaoui, A. Ben Fredj, S. Romdhane, M. Bouaïcha and H. Bouchriha, Enhancement of magneto-conductance in n-Si/n-PS/NPB structures at room temperature, *Mater. Sci. Eng. B*, 2013, **178**, 1416–1421.

6 B. Chouaibi, M. Radaoui, A. Ben Fredj, S. Romdhane, M. Bouaïcha and H. Bouchriha, Electrical conductance and magnetoconductance effect on n-type porous silicon: Contribution of weak localization correction, *Superlattices Microstruct.*, 2015, **85**, 680–689.

7 V. Schmidt, H. Riel, S. Senz, S. Karg, W. Riess and U. Gösele, Realization of a Silicon Nanowire Vertical Surround-Gate Field-Effect Transistor, *Small*, 2006, **2**, 85–88.

8 J. Goldberger, A. I. Hochbaum, R. Fan and P. Yang, Silicon Vertically Integrated Nanowire Field Effect Transistors, *Nano Lett.*, 2006, **6**, 973–977.

9 B. Tian, X. Zheng, T. J. Kempa, Y. Fang, N. Yu, G. Yu, J. Huang and C. M. Lieber, Coaxial silicon nanowires as solar cells and nanoelectronic power sources, *Nature*, 2007, **449**, 885–889.

10 Y. Cui, Z. Zhong, D. Wang, W. U. Wang and C. M. Lieber, High Performance Silicon Nanowire Field Effect Transistors, *Nano Lett.*, 2003, **3**, 149–152.

11 G. Zheng, W. Lu, S. Jin and C. M. Lieber, Synthesis and Fabrication of High-Performance n-Type Silicon Nanowire Transistors, *Adv. Mater.*, 2004, **16**, 1890–1893.

12 H. Yan, H. S. Choe, S. Nam, Y. Hu, S. Das, J. F. Klemic, J. C. Ellenbogen and C. M. Lieber, Programmable nanowire circuits for nanoprocessors, *Nature*, 2011, **470**, 240–244.

13 C. K. Chan, H. Peng, G. Liu, K. McIlwrath, X. F. Zhang, R. A. Huggins and Y. Cui, High-performance lithium battery anodes using silicon nanowires, *Nature Nanotech*, 2008, **3**, 31–35.

14 M. D. Kelzenberg, S. W. Boettcher, J. A. Petykiewicz, D. B. Turner-Evans, M. C. Putnam, E. L. Warren, J. M. Spurgeon, R. M. Briggs, N. S. Lewis and H. A. Atwater, Enhanced absorption and carrier collection in Si wire arrays for photovoltaic applications, *Nature Mater*, 2010, **9**, 239–244.

15 K. Peng, X. Wang and S.-T. Lee, Silicon nanowire array photoelectrochemical solar cells, *Appl. Phys. Lett.*, 2008, **92**, 163103.

16 X. Wang, K.-Q. Peng, X.-J. Pan, X. Chen, Y. Yang, L. Li, X.-M. Meng, W.-J. Zhang and S.-T. Lee, High-Performance Silicon Nanowire Array Photoelectrochemical Solar Cells through Surface Passivation and Modification, *Angew. Chem., Int. Ed.*, 2011, **50**, 9861–9865.

17 G. Zheng, F. Patolsky, Y. Cui, W. U. Wang and C. M. Lieber, Multiplexed electrical detection of cancer markers with nanowire sensor arrays, *Nat. Biotechnol.*, 2005, **23**, 1294–1301.

18 F. Patolsky, G. Zheng and C. M. Lieber, Fabrication of silicon nanowire devices for ultrasensitive, label-free, real-time detection of biological and chemical species, *Nat. Protoc.*, 2006, **1**, 1711–1724.

19 B. Tian, T. Cohen-Karni, Q. Qing, X. Duan, P. Xie and C. M. Lieber, Three-Dimensional, Flexible Nanoscale Field-Effect Transistors as Localized Bioprobes, *Science*, 2010, **329**, 830–834.

20 Q. Qing, S. K. Pal, B. Tian, X. Duan, B. P. Timko, T. Cohen-Karni, V. N. Murthy and C. M. Lieber, *Nanowire Transistor Arrays for Mapping Neural Circuits in Acute Brain Slices*, Proceedings of the National Academy of Sciences, 2010, 107, 1882–1887.

21 F. Demami, L. Ni, R. Rogel, A. C. Salaun and L. Pichon, Silicon nanowires synthesis for chemical sensor applications, *Procedia Eng.*, 2010, **5**, 351–354.

22 R. Juhasz, K. Kylmänen, A. Galeckas and J. Linnros, Size-reduced silicon nanowires: Fabrication and electrical characterization, *Mater. Sci. Eng. C*, 2005, **25**, 733–737.

23 H.-P. Phan, T. Kozeki, T. Dinh, T. Fujii, A. Qamar, Y. Zhu, T. Namazu, N.-T. Nguyen and D. V. Dao, Piezoresistive effect of p-type silicon nanowires fabricated by a top-down process using FIB implantation and wet etching, *RSC Adv.*, 2015, **5**, 82121–82126.

24 D. S. Engstrom and Y.-A. Soh, Controlling the silicon nanowire tapering angle in dense arrays of silicon nanowires using deep reactive ion etching, *J. Vac. Sci. Technol. B*, 2013, **31**, 021806.

25 N. Nafie, M. Abouda Lachiheb, M. Ben Rabha, W. Dimassi and M. Bouaïcha, Effect of the doping concentration on the properties of silicon nanowires, *Phys. E Low-dimens. Syst. Nanostruct.*, 2014, **56**, 427–430.

26 G. Farid, R. Amade-Rovira, Y. Ma, S. Chaitoglou, R. Ospina and E. Bertran-Serra, Revolutionizing energy storage: Silicon nanowires (SiNWs) crafted through metal-assisted chemical etching, *Arab. J. Chem.*, 2024, **17**(13), 105631.

27 R. Plugaru, E. Fakhri, C. Romanitan, I. Mihalache, G. Craciun, N. Plugaru, H. Ö. Árnason, M. T. Sultan, G. A. Nemnes, S. Ingvarsson, H. G. Svavarsson and A. Manolescu, Structure and electrical behavior of silicon nanowires prepared by MACE process, *Surf. Interfaces*, 2022, **33**, 102167.

28 A. Boukhachem, C. Bouzidi, R. Boughalmi, R. Ouerteni, M. Kahlaoui, B. Ouni, H. Elhouichet and M. Amlouk, Physical investigations on MoO3 sprayed thin film for selective sensitivity applications, *Ceram. Int.*, 2014, **40**, 13427–13435.

29 A. B. Hafsia, N. Rammeh, M. Farid and M. Khitouni, Electrical conductivity and dielectric study of LaBaFe0.5Zn0.5MnO6−δ compound, *Ceram. Int.*, 2016, **42**, 3673–3680.

30 N. Sdiri, H. Elhouichet, B. Azeza and F. Mokhtar, Studies of (90-x) P2O5xB2O310Fe2O3 glasses by Mossbauer effect and impedance spectroscopy methods, *J. Non-Cryst. Solids*, 2013, **371–372**, 22–27.

31 K. Rasool, M. A. Rafiq, C. B. Li, E. Krali, Z. A. K. Durrani and M. M. Hasan, Enhanced electrical and dielectric properties of polymer covered silicon nanowire arrays, *Appl. Phys. Lett.*, 2012, **101**, 023114.

32 J.-J. Wu and D. K.-P. Wong, Fabrication and Impedance Analysis of n-ZnO Nanorod/p-Si Heterojunctions to Investigate Carrier Concentrations in Zn/O Source- Ratio-Tuned ZnO Nanorod Arrays, *Adv. Mater.*, 2007, **19**, 2015–2019.

33 R. Kumar and N. Khare, Temperature dependence of conduction mechanism of ZnO and Co-doped ZnO thin films, *Thin Solid Films*, 2008, **516**, 1302–1307.

34 A. Shukla, R. N. P. Choudhary and A. K. Thakur, Thermal, structural and complex impedance analysis of Mn4+ modified BaTiO3 electroceramic, *J. Phys. Chem. Solids*, 2009, **70**, 1401–1407.

35 C. Kittel, *Introduction to Solid State Physics*, Wiley, Hoboken, NJ, 8th edition., 2004.

36 A. Ben Rhaiem, F. Hlel, K. Guidara and M. Gargouri, Electrical conductivity and dielectric analysis of AgNaZnP2O7 compound, *J. Alloys Compd.*, 2009, **485**, 718–723.

37 M. Hsini, N. Hamdaoui, S. Hcini, M. L. Bouazizi, S. Zemni and L. Beji, Effect of iron doping at Mn-site on complex impedance spectroscopy properties of Nd0.67Ba0.33MnO3 perovskite, *Phase Transitions*, 2018, **91**, 316–331.

38 C. L. Alexander, B. Tribollet and M. E. Orazem, Contribution of Surface Distributions to Constant-Phase-Element (CPE) Behavior: 1. Influence of Roughness, *Electrochim. Acta*, 2015, **173**, 416–424.

39 A. Selmi, S. Hcini, H. Rahmouni, A. Omri, M. L. Bouazizi and A. Dhahri, Synthesis, structural and complex impedance spectroscopy studies of Ni0.4Co0.4Mg0.2Fe2O4 spinel ferrite, *Phase Transitions*, 2017, **90**, 942–954.

40 A. K. Jonscher, The 'universal' dielectric response, *Nature*, 1977, **267**, 673–679.

41 M. Radaoui, A. Ben Fredj, S. Romdhane, N. Bouguerra, D. A. M. Egbe and H. Bouchriha, New conjugated polymer/fullerene nanocomposite for energy storage and organic solar cell devices: Studies of the impedance spectroscopy and dielectric properties, *Synth. Met.*, 2022, **283**, 116987.

42 M. Radaoui, E. Hleli, Z. Ben Hamed, A. Ben Fredj, H. Hrichi, S. Romdhane, D. A. M. Egbe and H. Bouchriha, Spectroscopic characterization of a red light-emitting polymer: Anthracene-containing poly(p-arylene-ethynylene)-alt-poly(p-arylene-vinylene), *Mater. Sci. Semicond. Process.*, 2015, **30**, 285–291.

43 S. Hcini, A. Omri, M. Boudard, M. L. Bouazizi, A. Dhahri and K. Touileb, Microstructural, magnetic and electrical properties of Zn0.4M0.3Co0.3Fe2O4 (M = Ni and Cu) ferrites synthesized by sol–gel method, *J. Mater. Sci.: Mater. Electron.*, 2018, **29**, 6879–6891.

44 M. H. Dhaou, S. Hcini, A. Mallah, M. L. Bouazizi and A. Jemni, Structural and complex impedance spectroscopic studies of Ni0.5Mg0.3Cu0.2Fe2O4 ferrite nanoparticle, *Appl. Phys. A*, 2016, **123**, 8.

45 F. B. Abdallah, A. Benali, S. Azizi, M. Triki, E. Dhahri, M. P. F. Graça and M. A. Valente, Strontium-substituted La0.75Ba0.25−xSrxFeO3 (x = 0.05, 0.10 and 0.15) perovskite: dielectric and electrical studies, *J. Mater. Sci.: Mater. Electron.*, 2019, **30**, 8457–8470.

46 M. van Exter and D. Grischkowsky, Carrier dynamics of electrons and holes in moderately doped silicon, *Phys. Rev. B Condens. Matter*, 1990, **41**, 12140–12149.

47 X. Qian, N. Gu, Z. Cheng, X. Yang, E. Wang and S. Dong, Impedance study of (PEO)10LiClO4–Al2O3 composite polymer electrolyte with blocking electrodes, *Electrochim. Acta*, 2001, **46**, 1829–1836.

48 C. Rayssi, S. El. Kossi, J. Dhahri and K. Khirouni, Frequency and temperature-dependence of dielectric permittivity and electric modulus studies of the solid solution Ca0.85Er0.1Ti1−xCo4x/3O3 ($0 \leq x \leq 0.1$), *RSC Adv.*, 2018, **8**, 17139–17150.

49 X. Li, W. Xu, Y. Zhang, D. Xu, G. Wang and Z. Jiang, Chemical grafting of multi-walled carbon nanotubes on metal phthalocyanines for the preparation of nanocomposites with high dielectric constant and low dielectric loss for energy storage application, *RSC Adv.*, 2015, **5**, 51542–51548.

50 L. Xie, X. Huang, Y. Huang, K. Yang and P. Jiang, Core@Double-Shell Structured BaTiO3–Polymer Nanocomposites with High Dielectric Constant and Low Dielectric Loss for Energy Storage Application, *J. Phys. Chem. C*, 2013, **117**, 22525–22537.

51 Q. Li, L. Chen, M. R. Gadinski, S. Zhang, G. Zhang, H. U. Li, E. Iagodkine, A. Haque, L.-Q. Chen, T. N. Jackson and Q. Wang, Flexible high-temperature dielectric materials from polymer nanocomposites, *Nature*, 2015, **523**, 576–579.

52 Y. Feldman, A. Puzenko and Y. Ryabov, in *Fractals, Diffusion, and Relaxation in Disordered Complex Systems*, John Wiley & Sons, Ltd, 2006, pp. 1–125.

53 M. H. Khan, S. Pal and E. Bose, Frequency-dependent dielectric permittivity and electric modulus studies and an empirical scaling in (100−x)BaTiO3/(x)La0.7Ca0.3MnO3 composites, *Appl. Phys. A*, 2015, **118**, 907–912.

54 U. Dash, S. Sahoo, P. Chaudhuri, S. K. S. Parashar and K. Parashar, Electrical properties of bulk and nano Li2TiO3 ceramics: A comparative study, *J. Adv. Ceram.*, 2014, **3**, 89–97.
55 M. Younas, L. L. Zou, M. Nadeem, N.- ur-Rehman, S. C. Su, Z. L. Wang, W. Anwand, A. Wagner, J. H. Hao, C. W. Leung, R. Lortz and F. C. C. Ling, Impedance analysis of secondary phases in a Co-implanted ZnO single crystal, *Phys. Chem. Chem. Phys.*, 2014, **16**, 16030–16038.
56 S. Karthickprabhu, G. Hirankumar, A. Maheswaran, R. S. Daries Bella and C. Sanjeeviraja, Influence of metals on the structural, vibrational, and electrical properties of lithium nickel phosphate, *Ionics*, 2015, **21**, 345–357.
57 V. Thakur, A. Singh, A. M. Awasthi and L. Singh, Temperature dependent electrical transport characteristics of BaTiO3 modified lithium borate glasses, *AIP Adv.*, 2015, **5**, 087110.
58 T. Jadli, A. Mleiki, H. Rahmouni, K. Khirouni, E. K. Hlil and A. Cheikhrouhou, Investigation of physical properties of manganite on example of Sm0.35Pr0.2Sr0.45MnO3, *Phys. B*, 2021, **600**, 412548.
59 P. Ganguly and A. K. Jha, Impedance spectroscopy analysis of Ba5NdTi3Nb7O30 ferroelectric ceramic, *Phys. B*, 2010, **405**, 3154–3158.
60 R. S. Gedam and D. D. Ramteke, Electrical, dielectric and optical properties of La2O3 doped lithium borate glasses, *J. Phys. Chem. Solids*, 2013, **74**, 1039–1044.
61 S. Rani, N. Ahlawat, R. Punia, K. M. Sangwan and P. Khandelwal, Dielectric and impedance studies of La and Zn co-doped complex perovskite CaCu3Ti4O12 ceramic, *Ceram. Int.*, 2018, **44**, 23125–23136.